

### Research Highlights

- Proposed wavelet-based topological loss function for image denoising .
- Tested on BVI-Lowlight dataset with real noise distortions.
- Achieved significant improvements in LPIPS metric, up to 25%.
- The loss function reserves textural information while removing noise.
- The novel loss is a promising approach for image enhancement techniques.



## Wavelet-based Topological Loss for Low-Light Image Denoising

Alexandra Malyugina<sup>a</sup>, Nantheera Anantrasirichai<sup>1</sup>, David Bull<sup>1</sup>

<sup>a</sup>*Visual Information Laboratory, University of Bristol, 1 Cathedral Square, Bristol, BS8 1UB, UK*

### ABSTRACT

Despite extensive research conducted in the field of image denoising, many algorithms still heavily depend on supervised learning and their effectiveness primarily relies on the quality and diversity of training data. It is widely assumed that digital image distortions are caused by spatially invariant Additive White Gaussian Noise (AWGN). However, the analysis of real-world data suggests that this assumption is invalid. Therefore, this paper tackles image corruption by real noise, providing a framework to capture and utilise the underlying structural information of an image along with the spatial information conventionally used for deep learning tasks. We propose a novel denoising loss function that incorporates topological invariants and is informed by textural information extracted from the image wavelet domain. The effectiveness of this proposed method was evaluated by training state-of-the-art denoising models on the BVI-Lowlight dataset, which features a wide range of real noise distortions. Adding a topological term to common loss functions leads to a significant increase in the LPIPS (Learned Perceptual Image Patch Similarity) metric, with the improvement reaching up to 25%. The results indicate that the proposed loss function enables neural networks to learn noise characteristics better. We demonstrate that they can consequently extract the topological features of noise-free images, resulting in enhanced contrast and preserved textural information.

© 2023 Elsevier Ltd. All rights reserved.

### 1. Introduction

Denoising is a common task when processing low-quality image data and forms an important component in the processing pipeline for cases where acquisition is performed under low light conditions. Applications include object detection and object tracking in autonomous vehicles, biomedical image analysis, natural history filmmaking and consumer video production. The primary objective of image denoising is to eliminate the noise present while preserving the original features. However, in practice denoising poses an inverse problem with intrinsically ambiguous solutions and hence always results in a trade-off between signal distortion and noise removal. Moreover, denoising methods should not introduce new artefacts, for example over smoothing (blurring), that can degrade the visual quality of the image.

Conventional denoising algorithms (pre machine learning), such as Non-Local Means (NLM) Buades et al. (2005) and

Block-Matching and 3D filtering (BM3D) Dabov et al. (2009), rely on mathematical models and involve pre-defined filters to remove noise from images. Latterly, state-of-the-art denoising methods have exploited deep learning-based approaches Anantrasirichai and Bull (2021a). Some methods have adopted a self-supervised learning framework to address the issue of unavailable ground truth data, e.g. Krull et al. (2019), Batson and Royer (2019), Ulyanov et al. (2018). However, the performance of these methods is limited, particularly for low-light content where, for example, edges are significantly distorted due to the presence of noise Anantrasirichai and Bull (2021b). The best-performing methods hence rely on supervised learning, where models are trained either by applying synthetic noise to the clean images or by creating pseudo ground truth data from real noise images Zhang et al. (2017) Anwar and Barnes (2019) Abdelhamed et al. (2020).

Deep learning approaches are typically developed by designing a network architecture and defining a loss function. In this paper, we focus on the latter. The loss function plays a critical role in measuring the performance of the neural network, and the goal of training is to minimise this loss. Through

\*\*Corresponding author: Tel.: +447383156544  
e-mail: [a.lex.malyugina@bristol.ac.uk](mailto:a.lex.malyugina@bristol.ac.uk) (Alexandra Malyugina)

the backpropagation algorithm, the loss function provides feedback to the neural network by computing its gradient, which is then used to update the network’s weights. Commonly used loss functions for image denoising include  $\ell_1$ ,  $\ell_2$ , Charbonnier, SSIM, Laplacian loss and a combination of these Abdelhamed et al. (2020). Other losses have also been employed, including perceptual loss, wavelet-based loss, gradient loss and total variation loss, but no performance improvement has been reported with these methods Anantrasirichai and Bull (2021b). Despite significant efforts to improve the performance of denoising methods, their results still typically exhibit distortion artifacts or lost signal information. Moreover, there are no reports that analyse how the loss function influences noise removal for different content classes. In this paper we introduce a novel loss function, combining local low level features and topological features extracted from the image. The denoising model is trained to be selective with respect to the textured areas of the image, resulting in improvements in contrast and performance on edges. Our proposed loss function is based on our previous work in Malyugina et al. (2023); we further enhance performance by using wavelets to categorise different content classes, such as homogeneous regions, edges, structures, and textures. We then create a weight map to apply the appropriate loss to each category. This is applied at the pixel level resulting in enhanced sharpness and spatial contrast in the output image. Additionally, we calculate topological invariants of the whole image instead of patches (as reported in Malyugina et al. (2023)). We compare the performance of the new loss function across popular denoising architectures, revealing that adding a topological term to conventional loss functions helps to improve subjective results by enhancing contrast while preserving texture. In conclusion, the main contributions of our paper are

- A novel denoising loss function that incorporates topological invariants and leverages textural information from the image wavelet domain. The proposed framework effectively integrates both the underlying structural information and spatial characteristics of images.
- Evaluation of the proposed loss function with multiple denoising models on the BVI-Lowlight dataset, which is specifically designed for real noise distortions in low light conditions.

The remainder of this paper is organised as follows. Problem statement and existing solutions are presented in Section 2. Details of topological invariants and the proposed loss function for image denoising are described in Section 3 and Section 4, respectively. The performance of the method is evaluated in Section 5, followed by the conclusions in Section 6.

## 2. Image Denoising Problem and Current Solutions

### 2.1. Image Denoising Problem

Given an image  $I^N$  corrupted by noise  $N$ , the goal is to obtain a denoised image  $I^O$  that accurately represents the underlying clean image  $I^C$ . Mathematically, this can be expressed as:

$$I^O = f_{\theta}(I^N, )$$

where  $f_{\theta}$  represents the denoising function or model that takes the noisy image as input and produces the denoised image as output. The noisy image  $I^N$  in this case is the result of some function (e.g. signal-dependent noise) of  $I^C$ :

$$I^N = \text{Noise}(I^C)$$

The task of denoising can then be formulated as an optimisation problem, where one searches for an optimal parameter set  $\theta = \{\theta_i\}_{i \in I}$  for a denoising model  $f_{\theta}$  through minimising loss function  $\mathcal{L}$ :

$$\hat{\theta} = \arg \min_{\theta} \mathcal{L}(f_{\theta}(I^N), I^C).$$

The denoising process aims to estimate the clean image  $I^C$  by suppressing or removing the noise component from the noisy image  $I^N$ . This involves leveraging statistical properties of the noise and exploiting the underlying structure and features present in the image.

### 2.2. Current Image Denoising Methods

Denoising methods can be categorised based on the domain they operate on and the type of approach employed.

In terms of the domain, denoising methods can be classified into spatial domain, transform domain, and hybrid (spatio-domain) methods. Spatial domain methods operate directly on the pixel values of an image. They include local methods such as mean filters, order-statistic filters, and adaptive filters. Non-local methods, like non-local means (NLM), take advantage of image self-similarity for denoising. Techniques such as steering kernel regression (SKR) Takeda et al. (2006) and Wiener filtering Wiener (1949) have been proposed to improve the performance of spatial filters in structured areas containing edges Tronicke and Böniger (2013).

Transform domain methods involve representing image patches using orthogonal basic functions and adjusting coefficients to denoise the image. Wavelet-based denoising methods have gained popularity due to their sparsity and multiresolution properties. Thresholding techniques, such as VISUShrink Donoho and Johnstone (1994) and BayesShrink Chipman et al. (1997), are commonly used in wavelet domain denoising Shui (2009) Yu and Sapiro (2011) Foi et al. (2007) Simoncelli and Adelson (1996) Mihcak et al. (1999).

Dual domain methods combine spatial and transform domain filtering. The BM3D algorithm, proposed by Dabov et al. Dabov et al. (2007), utilizes collaborative filtering in both the spatial and transform domains. It groups similar image patches, applies transform-domain shrinkage, and performs inverse transforms to obtain denoised images. Shape-adaptive versions of BM3D further improve the preservation of image details Dabov et al. (2008) Dabov et al. (2009).

In terms of the type of approach, denoising methods can be divided into conventional and learning-based methods. Conventional methods typically employ handcrafted algorithms and heuristics to remove noise from images. These approaches include filters such as mean filters, median filters, order-statistic

filters and many of the above-mentioned techniques (NLM, BM3D and thresholding).

Learning-based methods, such as sparse representation and dictionary learning, have been applied to image denoising. Techniques such as K-SVD Aharon et al. (2006) and locally learned dictionaries (K-LLD) Chatterjee and Milanfar (2009) utilise sparse coding and clustering techniques to represent image patches. The LSSC method proposed by Mairal et al. (2009) combines local and non-local sparsity within a neighborhood. Deep learning techniques, specifically convolutional neural networks (CNNs), have shown remarkable performance in image denoising. DnCNN, introduced by Zhang et al. (2017), is a deep neural network architecture based on residual learning that has achieved excellent results. One of state-of-the-art image denoising methods, RID-NET Anwar and Barnes (2019), utilise attention mechanisms with short and long connects to learn both local and global features. More recent learning-based denoisers combine transformer with UNet architectures, which enhances feature extraction and hierarchical representation capabilities Fan et al. (2022). The performance is comparable to RDUNet Gurrola-Ramos et al. (2021), where residual dense network is employed through UNet architectures.

It is worth noting that there is a distinction between supervised and unsupervised deep learning denoising. Supervised methods rely on ground truth images for training, while unsupervised methods aim to denoise images without ground truth information. Deep Image Prior Ulyanov et al. (2018) and Noise2Noise Lehtinen et al. (2018) are examples of unsupervised deep learning approaches, where networks are trained using only noisy input images. Conventional techniques often suffer from insufficient adaptability due to their reliance on fixed filters or predefined parameters, while learning-based denoising methods face challenges related to data requirements, generalization and handling new noise types. Both conventional and learning-based denoising approaches may encounter difficulties in preserving fine image details while reducing noise. However, learning-based algorithms have demonstrated better capabilities in addressing this challenge compared to conventional techniques.

### 3. Topological Invariants of Image Data

This section describes the mathematical concepts needed to create a topological loss function and to understand how can be exploited for image denoising.

Topological Data Analysis (TDA) has emerged as a powerful tool for analyzing complex data sets in various fields. It uses algebraic topology to study the shape and structure of data, including clusters, holes, and voids, which is particularly useful when dealing with data that may be high-dimensional or noisy. The TDA technique we employ here is called ‘*persistent homology*’, since it has been successfully applied to various problems, including genomics, material science, analysis of financial networks and image processing Byrne et al. (2023) Zomorodian and Carlsson (2005) Edelsbrunner et al. (2000) Epstein et al. (2011) Malyugina et al. (2022b) Carlsson et al. (2008).

In particular, the concept of persistent homology in TDA has shown promising results in topological image denoising Malyugina et al. (2023). It has been shown that, by applying a topological based loss function that operates in image patch space, noise removal can be enhanced while preserving essential topological features of the image.

Persistent homology can be used to deal with images by providing a robust and stable way to extract topological information from the image. By incorporating this information in the backpropagation process, persistent homology can assist in filtering out noise and extracting the underlying signal. The proposed loss function ensures that persistent homology features represented by persistent diagram of the denoised output of the neural network are close to those of the clean image.

TDA was originally derived for continuous curves and manifolds, making it unsuitable for discrete objects such as images. To identify and compute topological invariants, which are properties of geometric objects that remain constant under certain transformations, the concept of a simplicial complex is introduced. A simplicial complex consists of simple shapes of various dimensions like points, lines, triangles, and tetrahedrons. These shapes are arranged by significance using a technique called filtration, which orders them from simpler to more complex. The basic idea is to begin with the most straightforward simplicial complex, which generally includes unconnected points or vertices, and then systematically include additional simplices to the complex in a controlled manner. This allows us to study the evolution of the topology of the object as it becomes more complex.

**Definition 3.1** (Simplicial Complexes). Let  $V$  as a finite nonempty set, the elements of which are called vertices. A *simplicial complex* on  $V$  is a collection  $C$  of nonempty subsets of  $V$  that satisfies the following conditions:

- (i)  $\forall v \in V$ , the set  $\{v\}$  lies in  $C$ , and
- (ii)  $\forall \alpha \in C$ , and  $\beta \subseteq \alpha$ , where  $\beta$  is also an element of  $C$ .  $\alpha$  and  $\beta$  are called a *simplex* and a *face*, respectively.

Conditions (i) – (ii) mean that any face or subset of vertices of a simplex in the collection is also in the collection and the intersection of any two simplices in the collection is either empty or a face of both simplices.

The *dimension* of a simplex  $\alpha \in C$  is defined as  $\dim(\alpha) = |\alpha| - 1$ , the dimension of  $C$  is the highest dimension of constituent simplices.

In other words, a simplicial complex is a collection of simplices that fit together like puzzle pieces, where the boundaries of each simplex are shared with other simplices in the collection.

A *subcomplex* of a simplicial complex is a subset of its simplices that itself forms a simplicial complex. In other words, a subcomplex is a simplicial complex that is contained within another simplicial complex, or more formally,  $C'$  is called a *subcomplex* of  $C$ , if  $C' \subseteq C$  and  $C'$  is a simplicial complex itself. Intuitively, a subcomplex of a simplicial complex is a smaller “piece” of the original complex that retains its simplicial structure. For example, a triangle that is a face of a larger tetrahedron can be considered a subcomplex of that tetrahedron.

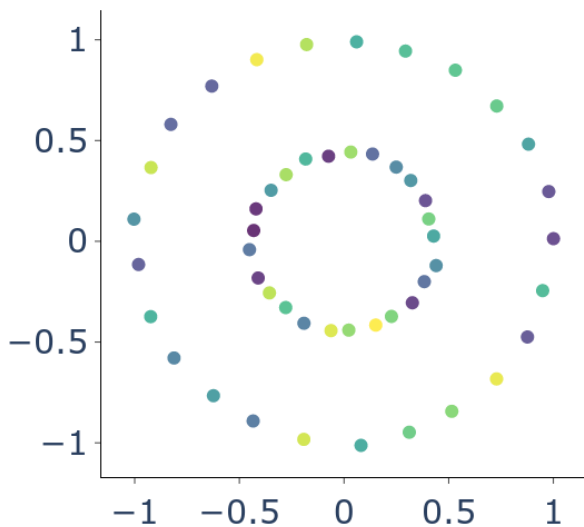
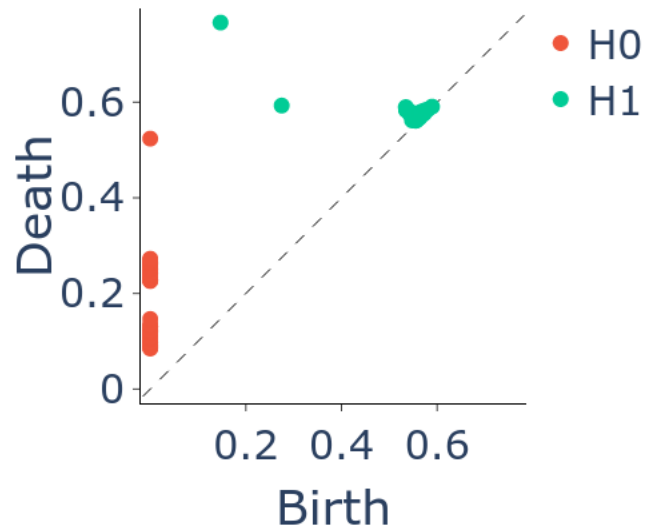
(a) Datacloud  $\mathcal{X}$ (b) Persistent diagram  $PD(\mathcal{X})$  for the datacloud  $\mathcal{X}$ .

Fig. 1: A persistent diagram  $PD(\mathcal{X})$  of a data cloud  $\mathcal{X}$  shows the birth (represented by the  $x$  coordinate) and death (represented by the  $y$  coordinate) of topological features of different dimensions (0-dimensional and 1-dimensional features, denoted as  $H_0$  and  $H_1$  respectively). Each point in the diagram corresponds to one of these features.

Simplicial complex is a general concept in topology that provides a structured way to study topological properties of spaces. One specific type of a simplicial complex used in topological data analysis is the Vietoris-Rips complex.

**Definition 3.2** (Vietoris-Rips Complex). Given a finite set of points  $P$  in a metric space  $(X, \rho)$  and a distance threshold  $\varepsilon > 0$ , the Vietoris-Rips complex  $V_\varepsilon(P)$  is a simplicial complex whose  $k$ -simplices correspond to subsets  $S \subseteq P$  with diameter  $\text{diam}(S)$  less than or equal to  $\varepsilon$ , i.e.,  $\text{diam}(S) = \max_{x,y \in S} \rho(x,y) \leq \varepsilon$ . Formally, a  $k$ -simplex  $S = \{p_0, p_1, \dots, p_k\}$  belongs to  $V_\varepsilon(P)$  if and only if  $\rho(p_i, p_j) \leq \varepsilon$  for all  $0 \leq i, j \leq k$ .

In other words, Vietoris-Rips complex is constructed from a set of data points by connecting those points that are within a certain distance threshold of each other. This type of complexes is useful for analyzing the shape and clustering of multi dimensional data, revealing different levels of detail as  $\varepsilon$  changes.

There are other types of widely used complexes in topological analysis. One of them, a cubical complex, specifically caters the data structure of digital images Choe and Ramanna (2022). Cubical complexes provide a different approach by utilising the structure composed of axis-parallel cubes that encapsulate the geometry and relationships between cells of varying dimensions in a more grid-like manner.

However, although cubical complexes are useful for digital image data Choe and Ramanna (2022), they have inherent higher-dimensional nature and the larger number of possible interactions between cells. This results in increased computational overhead and slower processing times compared to the relatively simpler pairwise distance calculations used in the

Vietoris-Rips complex construction. Computation times for RGB image patches are shown in Figure 2. For example, for  $512 \times 512$  patch, the computation time for cubical complex (the computation time is the same for 0- and 1- dimensions due to the algorithm) is  $\sim 5$  times higher than for 1-dim Vietoris-Rips and  $\sim 170$  times higher than for 0-dim Vietoris-Rips complex (computed on Nvidia 2080 Ti). Due to this considerable limitation and critical importance of the balance of computational speed and image patch size for deep-learning based denoising, throughout this paper we will assume the use of Vietoris-Rips complexes.

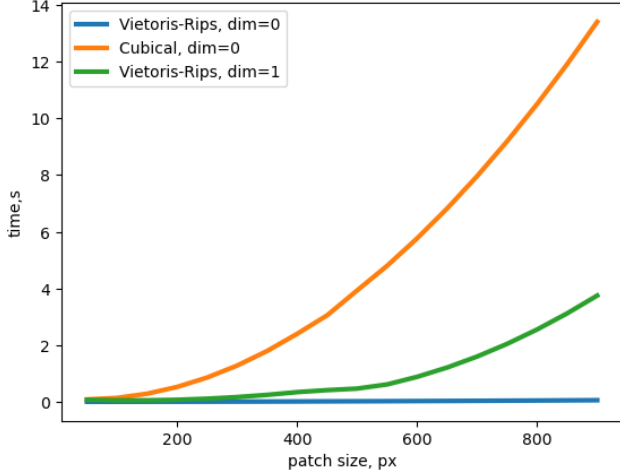
Simplices in a simplicial complex are arranged by significance using a technique called *filtration*.

**Definition 3.3** (Filtrations). A ( $n$ -)filtration of a simplicial complex is a sequence of subcomplexes, ordered by inclusion, such that each subcomplex is contained in the next. In other words, it is a sequence of simplicial complexes:

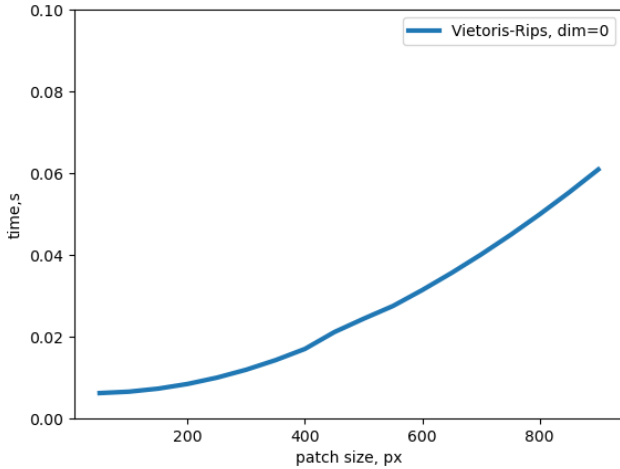
$$\mathcal{FC}_0 \subset \mathcal{FC}_1 \subset \mathcal{FC}_2 \cdots \subset \mathcal{FC}_n = \mathcal{C} \quad (1)$$

In TDA, while simplicial complexes are a convenient way to represent the connectivity and topological relationships within data, a filtration is used to provide a hierarchical representation of these relationship, revealing the evolution and persistence of topological features across different scales.

The purpose of filtrations is to capture the occurrence (“birth”) and disappearance (“death”) of topological like homology classes Edelsbrunner et al. (2000), that can emerge and vanish as the parameter  $\varepsilon$  of the filtration  $C_\varepsilon$  changes (for Vietoris-Rips complexes).



(a)



(b)

Fig. 2: (a) Computation times of Vietoris-Rips complexes and Cubical complexes of dimensions 0 and 1. (b) Computation times of Vietoris-Rips complex of dimension 0.

To visualise the changes in the topology of a simplicial complex over a range of filtration scales, a persistent diagram is created. The diagram displays each homology class Edelsbrunner et al. (2000) as a point, where the horizontal axis and the vertical axis represent the “birth” and “death” times, respectively.

**Definition 3.4** (Persistent diagrams). A *persistent diagram* of a filtration  $\mathcal{F}$  on a  $n$ -dimensional complex  $C$  is a collection of mappings  $PD = \{PD_k\}_{k=1}^{m \leq n}$ , each of which map every  $i^{\text{th}}$   $k$ -dimensional topological feature to a pair  $(b_i, d_i) \in \mathbb{R}^2 \cup \infty$ :

$$PD_k : (C, \mathcal{F}) \rightarrow \{b_i, d_i\}_{i \in I_k}, \quad (2)$$

where  $b_i$  represents the appearance (“birth”) of the feature when  $\varepsilon = b_i$  and  $d_i$  represents its disappearance (“death”) when  $\varepsilon = d_i$  (see Fig. 1). When  $k = 0$ , each point in the persistent diagram represent a connected component and when  $k = 1$ , a point corresponds to a 1-dimensional holes in filtered subcomplexes of  $C$ .

For image data, we calculate persistent diagrams on the filtrations of Vietoris-Rips complexes over image intensity scale, tracking the occurrence and disappearance of topological features at different intensity values. For our task, we consider  $k = 0$  to represent the number of connected components and  $k = 1$  to represent the number of 1-dimensional holes in filtered subcomplexes of  $C$ . As this paper focuses on specific aspects of the topic and cannot accommodate a comprehensive discussion of concepts such as homology classes and groups, we refer the readers to Edelsbrunner et al. (2000) for more theoretical foundations and a deeper theoretical understanding of persistent diagrams.

## 4. Wavelet-based Topological Loss Function

### 4.1. Topological Loss Function

To construct a topological loss for a pair of ground truth and output images  $(\mathcal{I}^C, \mathcal{I}^O)$ , we first calculate persistence diagrams  $PD(\mathcal{I}^C)$  and  $PD(\mathcal{I}^O)$  using intensity-based filtrations of Vietoris-Rips complexes calculated in the spatial dimension of the images. The topological distance between two diagrams is then calculated using total persistence as a dissimilarity measure.

**Definition 4.1** (Total Persistence). *p*-total persistence of a persistence diagram  $PD$  is defined as a total sum of the lifespans of each point in a diagram:

$$TPers(PD) = \sum_{x \in PD} (d(x) - b(x))^p, \quad (3)$$

where  $d(x)$  and  $b(x)$  are “death” and “birth” values of  $x \in PD$ . For our experiments we use  $p = 1$ .

Total persistence can be interpreted as the overall importance of topological features in a simplicial complex over a range of filtration scales.

Finally, we can use total persistence as the dissimilarity measure for the persistence diagrams space. We introduce the topological component of our future loss function, that we define

as shown in Eq. 4, where the absolute value is used instead of squaring to ensure robustness to outliers:

$$\mathcal{L}_{top}(\mathcal{I}^O, \mathcal{I}^C) = |TPers(PD(\mathcal{I}^O)) - TPers(PD(\mathcal{I}^C))|. \quad (4)$$

A topological loss function based on persistent homology in the space of contrast patches sampled spatially from an image was shown to improve image denoising task by Malyugina et al. in Malyugina et al. (2023). Unlike Malyugina et al. (2023), in this work we obtain topological information directly from the image spatial domain, leading to increased information of both local and global features. We then combine it with a spatial loss to ensure that local spatial information is retained. We used `torch-topological`<sup>1</sup> for calculation of complexes, filtrations and persistence diagrams.

#### 4.2. Texture Mask

In our experiments with  $\mathcal{L}_{top}$  defined in Equation 4, we observed that the topological loss component works better in textured areas or on edges, while sometimes creating undesired artifacts in plain untextured areas (see Fig. 5). Therefore we modified our approach to train and apply topological loss using a texture mask based on wavelet decompositions. Wavelets have been proven to be successful in capturing textual information in images through various applications, including texture classification Anantrasirichai et al. (2015a) and image denoising with texture preservation Hill et al. (2015). The patterns and variations in the wavelet coefficients can provide information about the spatial frequency content and orientation of the texture.

The Discrete Wavelet Transform (DWT) decomposes a signal into a set of mutually orthogonal basis wavelet functions. To retrieve textured areas from the ground truth image  $\mathcal{I}^C$ , we first apply 1-level decomposition with Haar base functions Schmidt (1907) and take only low frequency bands,  $LL$ . This aims to ignore the areas with fine textural detail and noise Anantrasirichai et al. (2015b), producing a smoother mask. Subsequently, we apply another DWT to  $LL$  and retrieve absolute values from the high-pass subbands  $HH, HV, HD$  of  $LL$ , where  $HH, HV$  and  $HD$  denote high-pass subbands in horizontal, vertical and diagonal directions, respectively. Finally, we take mean values of these three level 2 DWT subbands, thus resulting in a *texture mask* (see Fig. 3):

$$Mask(\mathcal{I}^C) = \text{mean}\{d_H\}_{H \in \{HH, HV, HD\}},$$

where

$$d_H = |DWT_{LL} \circ DWT_H \circ \uparrow_4(\mathcal{I}^C)|,$$

and  $\uparrow_4$  denotes upscaling with the factor of 4 and  $\circ$  is a function superposition.

Finally, to apply topological loss only to textured areas, we apply the texture mask to the image  $\mathcal{I}^C$ , producing  $Mask(\mathcal{I}^C)$

and combine it with pixelwise basic loss  $\mathcal{L}_{base}$ , where  $\mathcal{L}_{base} = \ell_1$  or  $\ell_2$ :

$$\mathcal{L}_{wvcomb}(\mathcal{I}^O, \mathcal{I}^C) = \mathcal{L}_{top}(\mathcal{I}^O, \mathcal{I}^C) \odot Mask(\mathcal{I}^C) + \alpha \mathcal{L}_{base}(\mathcal{I}^O, \mathcal{I}^C) \odot (\mathbb{I} - Mask(\mathcal{I}^C))$$

where  $\odot$  is element-wise product and  $\alpha$  is a scalar hyperparameter. The respective method is shown in Algorithm 1.

Figure 4 shows the diagram of the proposed wavelet-based topological loss function. The restored image output of the denoising network is transformed into topological features, which are subsequently compared with those of the groundtruth,  $\mathcal{L}_{top}$ . The final loss function is a combination of  $\mathcal{L}_{top}$  and  $\mathcal{L}_{base}$  with the weighting determined by the textural information extracted from the wavelet domain.

## 5. Experiments and discussion

### 5.1. Dataset

We trained and tested the models on the BVI-Lowlight dataset Malyugina et al. (2022a, 2023), which was collected to overcome the limitations of existing denoising datasets in terms of variations in noise levels and diverse content with varying textures. This dataset consists of 31,800 14-bit images captured from 20 scenes using two cameras, Nikon D7000 and Sony A7SII, with ISO settings ranging from 100 to 25600 and 100 to 409600, respectively. We ensured consistent lighting conditions by using non-flickering LED lights. Pseudo ground truth images were generated by applying postprocessing techniques, including the removal of oversaturated pixels, intensity alignment, and image registration. Further details can be found in Malyugina et al. (2023).

### 5.2. Training

In our experiments, we employed both traditional and state-of-the-art architectures for our baselines: i) A residual-based denoising convolutional neural network (DnCNN) introduced in Zhang et al. (2017) by Zhang et al., which is a widely-used method for benchmarking deep image denoisers. ii) UNet, an encoder-decoder style fully convolutional network Ronneberger et al. (2015), which has been extensively used as a foundational framework for image denoising. iii) RIDNet, a single-stage blind real image denoising network that incorporates a feature attention mechanism Anwar and Barnes (2019).

We compared the proposed loss with other denoising losses, including conventional losses  $\ell_1$ ,  $\ell_2$ , and VGG loss ( $\alpha$  is set to 0.99942857 as in Johnson et al. (2016)). In our experiments, we set topological loss term gain  $\alpha$  to 0.004 as it demonstrated best performance on test sets. We also tested several combinations of losses and models.

All models presented in this paper were trained using 11K patches from the BVI-Lowlight dataset. The patches were sized 256×256, and we trained the models for 40 epochs. The initial learning rate was set to 0.0001, and the batch size was 16, which was limited by the memory capacity of our computing system.

<sup>1</sup><https://github.com/aidos-lab/pytorch-topological>

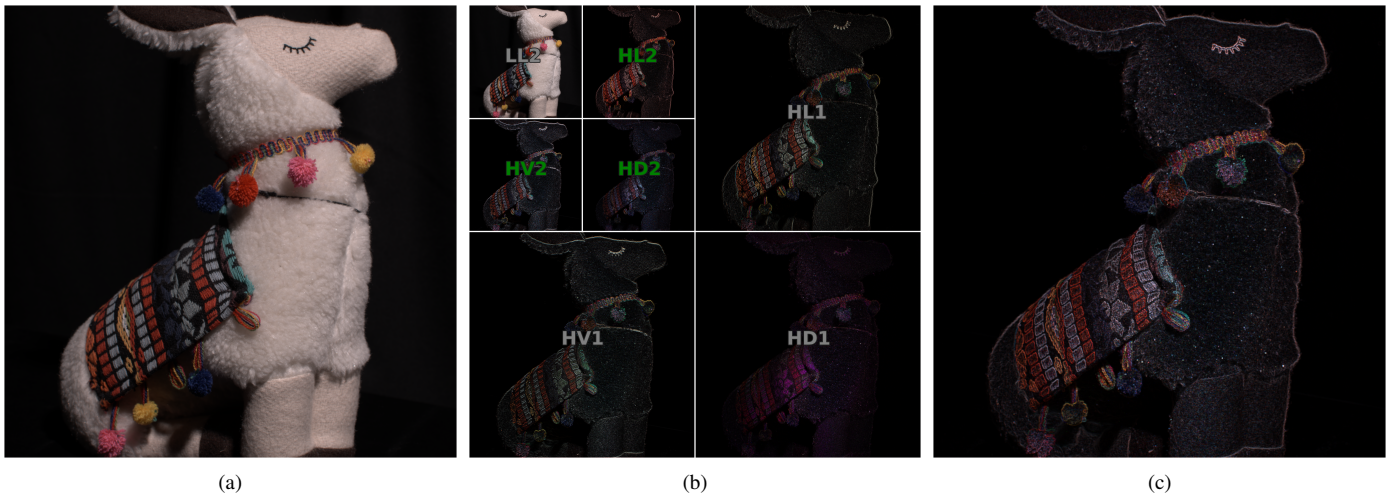


Fig. 3: (a) Ground truth image  $I^C$ ; (b) wavelet bands of 2-level decomposition  $DWT(I^C)$ ; (c) resulting wavelet mask  $Mask(I^C)$  built by averaging 2<sup>nd</sup> order high-pass bands (green in (b)).

### 5.3. Results

We evaluated the performance of our method by training state-of-the-art denoising models, using different loss functions and their combinations. The results based on objective metrics are presented in Table 1 and examples for subjective assessment are shown in Fig. 5 and Fig.6. These results demonstrate improved performance in terms of objective metrics that correlate more strongly with subjective quality assessment Zhang et al. (2018).

The highest and most consistent gain throughout all the architectures is achieved using the LPIPS metric: this shows improvements compared to conventional loss functions, as well as when combined with VGG. We have observed that perceptually, adding VGG loss in some cases helps to attenuate artifacts that can appear in plain areas when using masked topological loss only. Although with the RIDNET architecture, PSNR is lower for the models trained with topological loss compared to  $\ell_1$  or  $\ell_2$ , LPIPS values are still considerably higher. It is also worth noting that adding VGG loss term to a minimization criterion does not always improve the performance, comparing to models trained with basic loss only (see values for DnCNN with  $\ell_2$ ). Figure 5 shows that using a wavelet mask together with a topological term for the loss helps to reduce the occurrence of artifacts in homogeneous areas while preserving the texture and enhancing the contrast. For example, the denoised coin image using RIDNET with our proposed loss function exhibits sharper edges and better details compared to those denoised using  $\ell_2$  alone or without a mask. Additionally, RIDNET with the unmasked loss function fails to completely remove color noise.

Figure 6 shows the denoised results using DnCNN. The results obtained by training it with a topological loss are shown with wavelet-based masks. Comparing the results in the 5th and 6th rows to those in the 3rd and 4th rows, our proposed masked topological loss produces sharper results with better fine details. Specifically, the fonts in the third columns become more readable, such as ‘R61’. Without a topological loss, the VGG loss appears to remove the fine texture present in the top-right

area of the images in the fourth column, which is the white area of the lama’s doll fur. More subjective results are available in supplemental material, see Fig. 1.

Overall, the evaluation of the results based on the BVI-Lowlight dataset, featuring real-world noise levels, has demonstrated the effectiveness of the proposed loss function in enabling denoising models to better learn both noise characteristics and the underlying signal. This, in turn, leads to enhanced contrast and preserved textural information in the denoised images.

In the presence of noise, the topological properties of an image can become distorted or disrupted. By incorporating topological invariants into the loss function, the algorithm can effectively capture and preserve the original structural features of the image while removing the noise. This approach helps to maintain the integrity of textured areas, and enhance the overall visual quality of the denoised image, as well as provide a valuable framework for improving the performance of existing image denoising models and combating common problems such as oversmoothing.

## 6. Conclusion and Future Work

In this paper, we introduce a novel method for image denoising that incorporates a wavelet-based topological loss function and utilizes textural information from the image wavelet domain. Our proposed loss function effectively captures noise characteristics while preserving image texture, resulting in denoised images with enhanced visual quality and preserved perceptual fidelity of the original content. The experimental results on real noise confirm the efficacy of our method, showing superior perceptual results and improved performance in objective metrics that are highly correlated with subjective quality assessment.

For future research, the generalisability of the wavelet-based topological loss function should be further investigated across diverse datasets and noise types. Additionally, investigating the



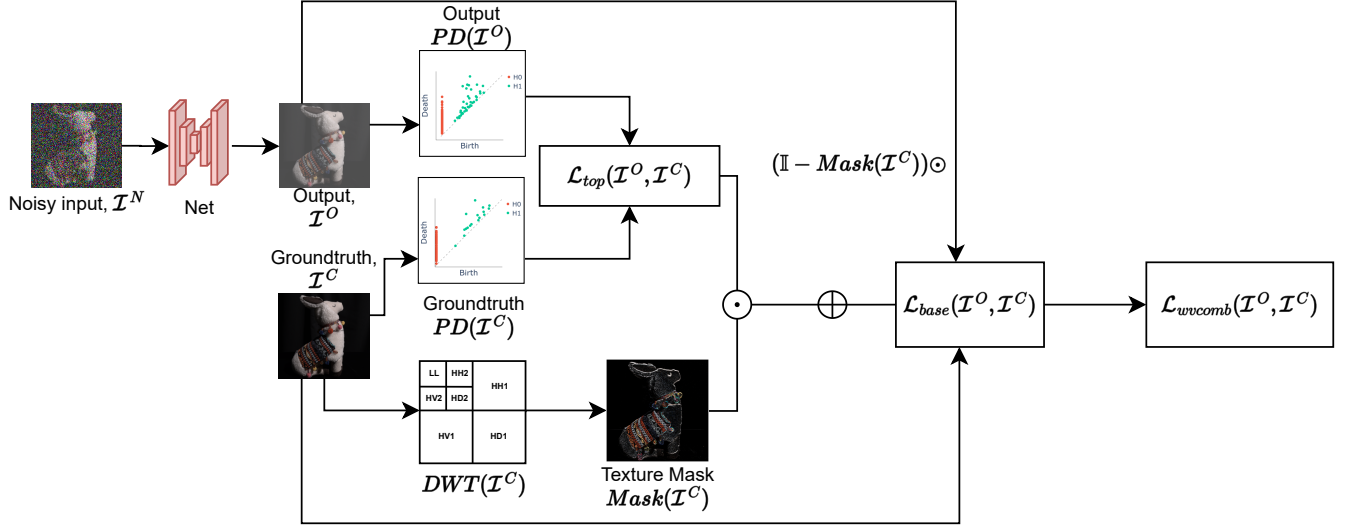


Fig. 4: Wavelet topological loss calculation for a pair of images: output image  $I^O$  and ground truth  $I^C$ . First, the texture mask of  $I^C$  is calculated based on wavelet decomposition of ground truth image  $I^C$ . The topological loss component  $\mathcal{L}_{top}$  is calculated as the absolute difference of total persistence values of diagrams  $PD(I_C)$  and  $PD(I_O)$ . We also calculate  $\mathcal{L}_{base}$  ( $l_1$  loss) to retain image spatial information. The resulting wavelet combined loss  $\mathcal{L}_{wvcomb}$  is calculated as pixelwise mask-weighted base loss  $M(I^C) \times \mathcal{L}_{top}$  and  $\mathcal{L}_{base}$ .

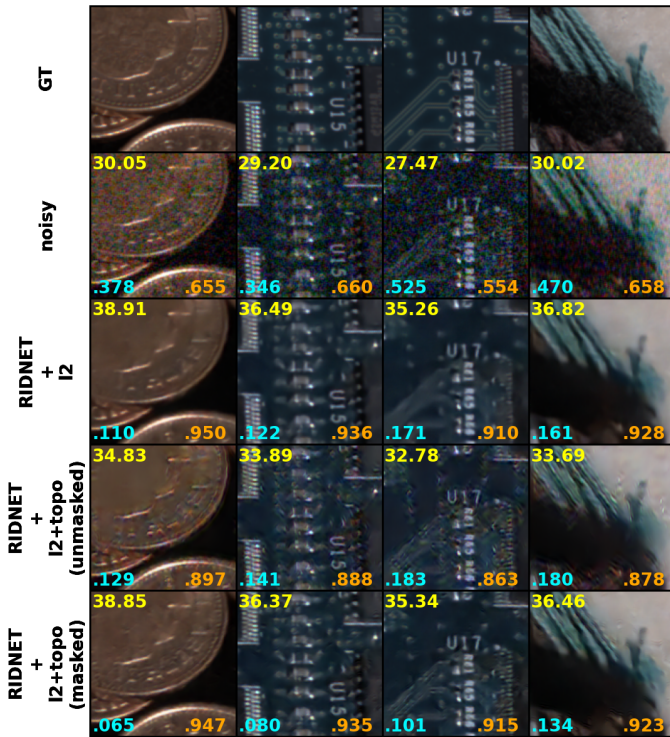


Fig. 5: Using wavelet mask with  $\mathcal{L}_{top}$ . *Top row*: Sample patches from dataset ground truth. *Second row*: Sample patches from noisy images with ISO varying from 160000 to 400000. *Third row*: Sample patches of the outputs from RIDNET trained with  $l_1$  only. *Fourth row*: Sample patches of the outputs from DnCNN trained with topology loss (unmasked) combined with  $l_1$ . *Bottom row*: Sample patches of the outputs from DnCNN trained with topology loss (masked) combined with  $l_1$ . PSNR (yellow), LPIPS (cyan) and SSIM (orange) values are calculated per corresponding pairs. Note the preserved edges, enhanced contrast and improvement in LPIPS metric values when using masked topological loss compared to  $l_1$  loss only. Using wavelet texture mask also prevents the network from producing undesirable artifacts.

integration of this approach with other denoising methods may yield further improvements.

## Acknowledgments

This work was supported by the UKRI MyWorld Strength in Places Programme (SIPF00006/1) and Bristol+Bath Creative R+D under AHRC grant (AH/S002936/1).

## References

- Abdelhamed, A., Afifi, M., Timofte, R., Brown, M.S., 2020. NTIRE 2020 Challenge on Real Image Denoising: Dataset, Methods and Results, in: Proceedings of the IEEE/CVF Conference on Computer Vision and Pattern Recognition (CVPR) Workshops.
- Aharon, M., Elad, M., Bruckstein, A., et al., 2006. K-SVD: An algorithm for designing overcomplete dictionaries for sparse representation. *IEEE Transactions on signal processing* 54, 4311.
- Anantrasirichai, N., Bull, D., 2021a. Artificial intelligence in the creative industries: a review. *Art. Int. Rev.*
- Anantrasirichai, N., Bull, D., 2021b. Contextual colorization and denoising for low-light ultra high resolution sequences, in: *ICIP proc.*, pp. 1614–1618.
- Anantrasirichai, N., Burn, J., Bull, D., 2015a. Terrain classification from body-mounted cameras during human locomotion. *IEEE Transactions on Cybernetics* 45, 2249–2260. doi:10.1109/TCYB.2014.2368353.
- Anantrasirichai, N., Burn, J., Bull, D.R., 2015b. Robust texture features based on undecimated dual-tree complex wavelets and local magnitude binary patterns, in: 2015 IEEE International Conference on Image Processing (ICIP), pp. 3957–3961. doi:10.1109/ICIP.2015.7351548.
- Anwar, S., Barnes, N., 2019. Real image denoising with feature attention. *IEEE International Conference on Computer Vision (ICCV-Oral)*.
- Batson, J., Royer, L., 2019. Noise2self: Blind denoising by self-supervision, in: *ICML proc.*, PMLR. pp. 524–533.
- Buades, A., Coll, B., Morel, J.M., 2005. A non-local algorithm for image denoising, in: *CVPR proc.*, IEEE. pp. 60–65.
- Byrne, N., Clough, J.R., Valverde, I., Montana, G., King, A.P., 2023. A persistent homology-based topological loss for CNN-based multiclass segmentation of CMR. *IEEE Transactions on Medical Imaging* 42, 3–14. URL: <https://doi.org/10.1109/2Ftmi.2022.3203309>, doi:10.1109/tmi.2022.3203309.

**Algorithm 1: Wavelet Topological Image Denoising**

**Input** : Noisy image  $I^N$ , Groundtruth image  $I^C$ ,  
Trainable model  $f_\theta$

**Output**: Optimised parameter set  $\hat{\theta}$

**Step 1: Wavelet Decomposition;**

Perform wavelet decomposition on  $I^C$  to obtain  $LL$  band wavelet coefficients;  $I_{LL}^C = DWT_{LL}(I^C)$

**Step 2: Texture Mask Calculation;**

Calculate the texture mask;  $Mask(I^C) = DWT_H(I_{LL}^C)$

**Step 3: Acquire model output  $I^O$ ;**

Apply model  $f_\theta$  to noisy image:  $I^O = f_\theta(I^N)$

**Step 4: Persistence Diagram Calculation;** Calculate the persistence diagrams  $PD(I^C)$  and  $PD(I^O)$  of  $I^C$  and  $I^O$ , respectively;

**Step 5: Topological Loss Term Calculation;**

Calculate the total persistence values  $TPers(I^C)$  and  $TPers(I^O)$  for  $PD(I^C)$  and  $PD(I^O)$ , respectively;  
Calculate the topological loss component  $\mathcal{L}_{top}$ :

$$\mathcal{L}_{top}(I^O, I^C) = |TPers(PD(I^O)) - TPers(PD(I^C))|;$$

**Step 6: Base Loss Term Calculation;**

Calculate the base loss component  $\mathcal{L}_{base}$  as the  $\ell_p$  loss between  $I^C$  and  $I^O$ ;

$$\mathcal{L}_{base} = \|(I^O, I^C)\|_p, \quad p = 1 \text{ or } 2$$

**Step 7: Combined Loss Calculation;**

Calculate the pixelwise mask-weighted topological loss to enforce the topological guidance in textured areas:

$$\mathcal{L}_{top}^{masked} = \mathcal{L}_{top} \odot Mask(I^C);$$

and in remaining ‘‘plain’’ areas tune it down:

$$\mathcal{L}_{base}^{masked} = \mathcal{L}_{base} \odot (1 - Mask(I^C));$$

Calculate the combined wavelet loss  $\mathcal{L}_{wvcomb}$  as the ( $\alpha$ -weighted) sum of the mask-weighted losses with gain  $\alpha$ ;

$$\mathcal{L}_{wvcomb}(I^O, I^C) = \mathcal{L}_{base}^{masked} + \alpha \mathcal{L}_{top}^{masked}$$

**Step 8: Find the parameters of the network, minimising combined loss;**

$$\hat{\theta} = \arg \min_{\theta} \mathcal{L}_{wvcomb}(f_\theta(I^N), I^C)$$

**return**  $\hat{\theta}$ ;

Carlsson, G., Ishkhanov, T., Silva, V.D., Zomorodian, A., 2008. On the local behavior of spaces of natural images. *Int. j. of comp. vision* 76, 1–12.  
Chatterjee, P., Milanfar, P., 2009. Clustering-based denoising with locally learned dictionaries. *IEEE Transactions on Image Processing* 18, 1438–1451.

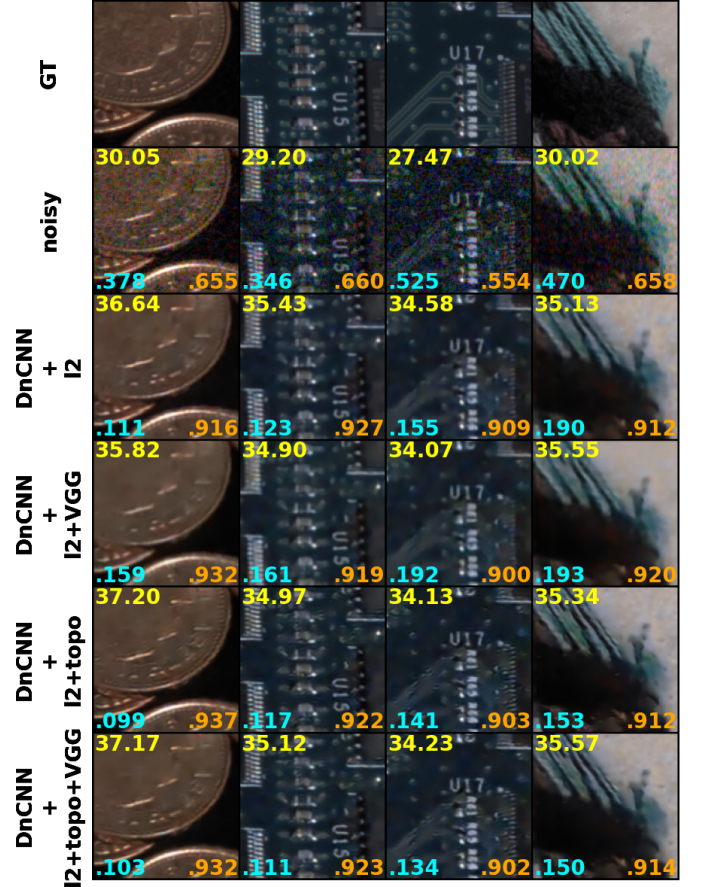


Fig. 6: Results. *Top row*: Sample patches from dataset ground truth. *Second row*: Sample patches from noisy images with ISO varying from 160000 to 400000. *Third row*: Sample patches of the outputs from DnCNN trained with  $\ell_1$  only. *Fourth row*: Sample patches of the outputs from DnCNN trained with VGG loss combined with  $\ell_1$ . *Fifth row*: Sample patches of the outputs from DnCNN trained with topology loss (masked) combined with  $\ell_1$ . *Bottom row*: Sample patches of the outputs from DnCNN trained with topology loss (masked) combined with VGG and  $\ell_1$ . PSNR (yellow), LPIPS (cyan) and SSIM (orange) values are calculated per corresponding pairs.

Chipman, H.A., Kolaczyk, E.D., McCulloch, R.E., 1997. Adaptive bayesian wavelet shrinkage. *Journal of the Amer. Stat. Assoc.* 92, 1413–1421.  
Choe, S., Ramanna, S., 2022. Cubical homology-based machine learning: An application in image classification. *Axioms* 11, 112.  
Dabov, K., Foi, A., Katkovnik, V., Egiazarian, K., 2007. Image denoising by sparse 3-d transform-domain collaborative filtering. *IEEE Transactions on image processing* 16, 2080–2095.  
Dabov, K., Foi, A., Katkovnik, V., Egiazarian, K., 2008. A nonlocal and shape-adaptive transform-domain collaborative filtering. *Proc. Int. Workshop on Local and Non-Local Approx. in Image Process.*, LNLA .  
Dabov, K., Foi, A., Katkovnik, V., Egiazarian, K., 2009. BM3D image denoising with shape-adaptive principal component analysis, in: *SPARS’09*.  
Donoho, D.L., Johnstone, J.M., 1994. Ideal spatial adaptation by wavelet shrinkage. *biometrika* 81, 425–455.  
Edelsbrunner, H., Letscher, D., Zomorodian, A., 2000. Topological persistence and simplification, in: *Proc. ann. symp. on found. of comp. sc.*, IEEE. pp. 454–463.  
Epstein, C., Carlsson, G., Edelsbrunner, H., 2011. Topological data analysis. *Inverse Problems* 27, 120201.  
Fan, C.M., Liu, T.J., Liu, K.H., 2022. Sunet: Swin transformer unet for image denoising, in: *2022 IEEE International Symposium on Circuits and Systems (ISCAS)*, pp. 2333–2337. doi:10.1109/ISCAS48785.2022.9937486.  
Foi, A., Katkovnik, V., Egiazarian, K., 2007. Pointwise shape-adaptive dct for high-quality denoising and deblocking of grayscale and color images. *IEEE Trans. on Image Proc.* 16, 1395–1411.

Table 1: Metrics values for the outputs of a corresponding model (DnCNN, RIDNET or UNet) trained with (i)  $\ell_i$  only (ii) combination of  $\ell_i$  with VGG loss (iii) combination of  $\ell_i$  with persistence-based loss  $\mathcal{L}_{top}$  (iv) combination of  $\ell_i$  with persistence-based loss  $\mathcal{L}_{top}$  and VGG loss  $\mathcal{L}_{vgg}$ .

|                    | LPIPS        | PSNR         | SSIM         |
|--------------------|--------------|--------------|--------------|
| Noisy              | 0.430        | 29.19        | 0.632        |
| DnCNN+l1           | 0.172        | 35.26        | 0.918        |
| DnCNN+l1+vgg       | 0.166        | 35.33        | 0.917        |
| DnCNN+l1+topo      | <b>0.129</b> | 35.60        | <b>0.923</b> |
| DnCNN+l1+topo+vgg  | 0.134        | <b>35.66</b> | 0.921        |
| DnCNN+l2           | 0.154        | 35.54        | <b>0.923</b> |
| DnCNN+l2+vgg       | 0.186        | 34.83        | 0.914        |
| DnCNN+l2+topo      | 0.131        | 35.42        | 0.918        |
| DnCNN+l2+topo+vgg  | <b>0.124</b> | <b>35.55</b> | 0.919        |
| RIDNET+l1          | 0.119        | 36.97        | 0.934        |
| RIDNET+l1+vgg      | 0.115        | 37.06        | 0.936        |
| RIDNET+l1+topo     | <b>0.096</b> | <b>37.24</b> | <b>0.938</b> |
| RIDNET+l1+topo+vgg | 0.108        | 37.23        | 0.937        |
| RIDNET+l2          | 0.098        | <b>37.30</b> | 0.937        |
| RIDNET+l2+vgg      | 0.098        | 37.23        | <b>0.939</b> |
| RIDNET+l2+topo     | 0.094        | 36.65        | 0.928        |
| RIDNET+l2+topo+vgg | <b>0.089</b> | 36.91        | 0.933        |
| UNet+l1            | 0.180        | 35.36        | 0.916        |
| UNet+l1+vgg        | 0.179        | 35.34        | 0.915        |
| UNet+l1+topo       | <b>0.136</b> | <b>35.68</b> | 0.923        |
| UNet+l1+topo+vgg   | 0.139        | 35.65        | <b>0.924</b> |
| UNet+l2            | 0.171        | 35.64        | 0.919        |
| UNet+l2+vgg        | 0.165        | 35.75        | 0.922        |
| UNet+l2+topo       | 0.121        | 35.82        | 0.919        |
| UNet+l2+topo+vgg   | <b>0.116</b> | <b>35.88</b> | <b>0.923</b> |

Gurrola-Ramos, J., Dalmau, O., Alarcón, T.E., 2021. A residual dense u-net neural network for image denoising. *IEEE Access* 9, 31742–31754. doi:10.1109/ACCESS.2021.3061062.

Hill, P., Anantrasirichai, N., Achim, A., Al-Mualla, M., Bull, D., 2015. Undecimated dual-tree complex wavelet transforms. *Signal Processing: Image Communication* 35, 61–70. URL: <https://www.sciencedirect.com/science/article/pii/S0923596515000715>, doi:<https://doi.org/10.1016/j.image.2015.04.010>.

- Johnson, J., Alahi, A., Fei Fei, L., 2016. Perceptual losses for real-time style transfer and super-resolution. *CoRR* abs/1603.08155. URL: <http://arxiv.org/abs/1603.08155>, arXiv:1603.08155.
- Krull, A., Buchholz, T.O., Jug, F., 2019. Noise2void-learning denoising from single noisy images, in: *CVPR* proc., pp. 2129–2137.
- Lehtinen, J., Munkberg, J., Hasselgren, J., Laine, S., Karras, T., Aittala, M., Aila, T., 2018. Noise2noise: Learning image restoration without clean data. arXiv preprint arXiv:1803.04189.
- Mairal, J., Bach, F., Ponce, J., Sapiro, G., Zisserman, A., 2009. Non-local sparse models for image restoration, in: *CVPR* proc., IEEE. pp. 2272–2279.
- Malyugina, A., Anantrasirichai, N., Bull, D., 2022a. Bvi-lowlight. URL: <https://dx.doi.org/10.21227/zp7a-0683>, doi:10.21227/zp7a-0683.
- Malyugina, A., Anantrasirichai, N., Bull, D., 2022b. A topological loss function: Image denoising on a low-light dataset. URL: <https://arxiv.org/abs/2208.04573>, doi:10.48550/ARXIV.2208.04573.
- Malyugina, A., Anantrasirichai, N., Bull, D., 2023. A topological loss function for image denoising on a new BVI-lowlight dataset. *Signal Processing*, 109081URL: <https://www.sciencedirect.com/science/article/pii/S016516842300155X>, doi:<https://doi.org/10.1016/j.sigpro.2023.109081>.
- Mihcak, M.K., Kozintsev, I., Ramchandran, K., Moulin, P., 1999. Low-complexity image denoising based on statistical modeling of wavelet coefficients. *IEEE Signal Processing Letters* 6, 300–303.
- Ronneberger, O., Fischer, P., Brox, T., 2015. U-net: Convolutional networks for biomedical image segmentation, in: *MICCAI*, Springer. pp. 234–241.
- Schmidt, E., 1907. Zur theorie der linearen und nichtlinearen integralgleichungen. *Mathematische Annalen* 63, 433–476.
- Shui, P.L., 2009. Image denoising using 2-d separable oversampled dft modulated filter banks. *IET Image processing* 3, 163–173.
- Simoncelli, E.P., Adelson, E.H., 1996. Noise removal via bayesian wavelet coring, in: *Proc. 3rd IEEE Intern. Conf. on Image Proc.*
- Takeda, H., Farsiu, S., Milanfar, P., et al., 2006. Kernel regression for image processing and reconstruction.
- Tronicke, J., Böniger, U., 2013. Steering kernel regression: An adaptive denoising tool to process gpr data, in: *Advanced Ground Penetrating Radar (IWAGPR)*, 2013 7th International Workshop on, IEEE. pp. 1–4.
- Ulyanov, D., Vedaldi, A., Lempitsky, V., 2018. Deep image prior, in: *CVPR* proc., pp. 9446–9454.
- Wiener, N., 1949. Extrapolation, interpolation and smoothing of stationary time series with engineering applications.
- Yu, G., Sapiro, G., 2011. DCT image denoising: a simple and effective image denoising algorithm. *Image Processing On Line* 1, 292–296.
- Zhang, K., Zuo, W., Chen, Y., Meng, D., Zhang, L., 2017. Beyond a gaussian denoiser: Residual learning of deep cnn for image denoising. *IEEE Transactions on Image Processing* 26, 3142–3155.
- Zhang, R., Isola, P., Efros, A.A., Shechtman, E., Wang, O., 2018. The unreasonable effectiveness of deep features as a perceptual metric, in: *CVPR*.
- Zomorodian, A., Carlsson, G., 2005. Computing persistent homology. *Disc. & Comp. Geometry* 33, 249–274.